ELECTRONIC SUPPLEMENTARY INFORMATION

Structure, bonding and ionic mobility in Na-V-P-O glasses for energy storage applications†

S.D. Wansi Wendji,[a,b,†] R. Piotrowski,[c,†] A. Familiari,[a,b,d] C. Massobrio,[b,e] M. Boero,[b,e] C. Tugène,[a] F. Shuaib,[c] D. Hamani,[c] P.-M. Geffroy,[c] P. Thomas,[c] A. Pedone,[d] A. Bouzid,[c] O. Masson,[c] G. Delaizir,[c] and Guido Ori*[a,b]

[a] *Université de Strasbourg, CNRS, Institut de Physique et Chimie des Matériaux de Strasbourg, UMR 7504, F-67034 Strasbourg, France.*
[b] *ADYNMAT CNRS consortium, F-67034 Strasbourg, France.*
[c] *Institut de Recherche sur les Céramiques, UMR 7315 CNRS-Univesité de Limoges, Centre Européen de la Céramique, 12 rue Atlantis 87068 Limoges Cedex, France*
[d] *Department of Chemical and Geological Sciences, University of Modena and Reggio Emilia, Modena, Italy*
[e] *Université de Strasbourg, CNRS, Laboratoire ICube, UMR 7357, Strasbourg, France.*

* *E-mail: guido.ori@cnrs.fr*
† These authors contributed equally to this work.

This Supplementary Information provides additional details on the experimental and computational methodologies employed in this work for the studied VP (V_xO_x–P_2O_5) and NVP (Na_2O–V_xO_x–P_2O_5) glass systems.

1 Experimental and computational methodologies

1.1 Glasses' synthesis

NVP10 and NVP28 glasses were prepared using sodium carbonate Na_2CO_3 (Strem Chemicals, 99.5%), vanadium pentoxide V_2O_5 (Strem Chemicals, 99.5%), and ammonium phosphate dibasic $(NH_4)_2HPO_4$ (Sigma-Aldrich, 98%) as raw materials. The precursors were weighed in appropriate amounts, mixed in an agate mortar, and heated in a platinum crucible to produce the two glass compositions. These are referred to as NVP10 and NVP28, respectively, based on the total vanadium content, as reported in Table S1. Note that in previous works, NVP28 (indicating the Na_2O content) was referred to as NVP43 (indicating the V_xO_y content).[1] A preliminary heat treatment at 300°C for 2h was required in order to decompose Na_2CO_3 and $(NH_4)_2HPO_4$. The temperature was then slowly raised at the heating rate of 5°C/min from room temperature up to 900°C. The melt was kept at this temperature for 1h with a homogenization each 15 min. The melt was quenched at room temperature between two stainless steel plates to get glass sample. Finally, all glass samples were annealed at T_g-10°C after melt-quenching to minimize thermal history effects on their properties.

1.2 Glasses' characterization

Note that the following characterization pertains to the two NVP glasses presented in this work. Part of this data have been previously reported in Wansi Wendji *et al.*[1] for NVP28. The experimental data used for comparison for NVP0 (denoted previously as VP50[2]) is taken from Hoppe *et al.*[3].

Density was measured on the glass powder using helium pycnometer (Micromeritics AccuPyc II 1340) in a 1 cm^3 cell. The thermal properties of the two glasses were determined using differential scanning calorimetry (DSC, model TA Instrument AQ20) from 40° to 550°C at 10 °C/min, allowing to determine the glass transition and crystallization temperatures (T_g and T_c, respectively), together with the thermal stability that is defined according to the Dietzel criterion as $\Delta T = T_c - T_g$. XPS measurements to determine the speciation of V sites were performed using a Kratos Axis Ultra DLD spectrometer with a monochromatic Al Kα source (12 mA, 15 kV). The working function of the instrument was calibrated to give a binding energy of the metallic gold Au $4f_{5/2}$ of 84.0 eV, and the dispersion was adjusted to give a binding energy of metallic copper Cu $2p_{3/2}$ at 932.6 eV. The Kratos charge neutralization system was used for each analysis, and still completed so as to set the V $2p_{3/2}$ (V^{5+}) signal at 517.2 eV. The pressure in the analysis chamber was around 5×10^{-9} Torr. Survey spectra were obtained over an analysis area of approximately 700x300 μm and a resolution of 160 eV (Pass Energy). High Resolution spectra were obtained over the same analysis area at a resolution of 20 eV (Pass Energy). The spectra were analyzed using CasaXPS software[4] (v. 2.3.25) with curves generally mixing 70% Gaussian and 30% Lorentzian, and Shirley mode for inelastic electron background subtraction.

The experimental total X-ray structure factor $S(k)$ and reduced total pair distribution functions $G(r)$ of our NVPs systems were determined through X-ray total scattering following procedures similar to those employed previously.[5] X-ray scattering measurements were conducted at room temperature using a specialized laboratory setup based on a Bruker D8 Advance diffractometer. This instrument was equipped with a silver sealed tube (λ = 0.559422 Å) and a rapid LynxEye XE-T detector to enable data collection with good counting statistics up to a large scattering vector length of 21.8 $Å^{-1}$. Approximately 20 mg of each sample's powder were placed in a thin-walled (0.01 mm) borosilicate glass capillary with a diameter of about 0.7 mm to limit absorption effects. The μR values (where R is the capillary radius and μ is the sample's linear attenuation coefficient) were estimated based on precise measurements of the mass and dimensions of the samples.[1] The raw data were corrected, normalized, and Fourier transformed using custom software[6] to obtain the reduced atomic pair distribution functions $G(r)$. Corrections accounted for capillary contributions, empty environment, Compton and multiple scatterings, absorption, and polarization effects. The necessary X-ray mass attenuation coefficients, atomic scattering factors, and Compton scattering functions for data correction and normalization were calculated from tabulated data provided by the DABAX database.[7] Absorption corrections were evaluated using a numerical midpoint integration method, where the sample cross-section was divided into small subdomains, following a method similar to that proposed by A. K. Soper and P. A. Egelstaf.[8]

Throughout the manuscript and the ESI, we present comparisons between experimental and simulated data for pair correlation functions, consistently formatted according to the experimental data reference. Specifically, we use the reduced pair distribution function $G(r)$ for NVP10 and NVP28, and the total correlation function $T(r)$ for NVP0, as reported by Hoppe et al.[3] and consistently with our previous works.[1,2]

The conductivity was determined by Electrochemical Impedance Spectroscopy (EIS) measurements with a Solartron 1260 Impedance/Gain-Phase Analyzer at frequencies ranging from 5 MHz to 1 Hz, and a voltage amplitude of 3 V. Impedance measurements were carried out during a heating stage from room temperature to about 20 °C below the glass transition temperature. The electronic conductivity (S/cm) was calculated using the equation σ = L/(R.S) where L is the pellet thickness (cm), R is the overall resistance (Ω), and S is the area of the pellet (cm^2).

Table S1 Chemical compositions (in mol (%) (with contributions from V_2O_4 and V_2O_5)) of Na_2O-V_xO_y-P_2O_5 glass systems NVP0, NVP10, and NVP28 synthesized and simulated.

Systems		n. atoms	Na_2O (%)	V_xO_y [V_2O_4 + V_2O_5] (%)	P_2O_5 (%)	V^{4+} (%)
NVP0	Exp.[a]	–	–	50.0 [17.6 + 32.4]	50.0	35.2[a]
	s-BOMD	218	–	50.0 [18.0 + 31.7] [b]	50.0	35.9[b]
	CMD-BMP	218	–	50.0 [18.75 + 32] [c]	50.0	37.5[c]
	CMD-MLIP	218	–	50.0 [18.0 + 31.7] [d]	50.0	36.0[d]
	CMD-MLIP	5886	–	50.0 [– + –]	50.0	–
NVP10	Exp.[e]	–	10.0	40.0 [15.2 + 24.8] [f]	50.0	38.0[f]
	s-BOMD	388	10.0	40.0 [10.0 + 30.0] [b]	50.0	25.0[b]
	f-BOMD	388	10.0	40.0 [10.0 + 30.0] [b]	50.0	25.0[b]
	CMD-BMP	388	10.0	40.0 [13.20 + 26.8] [c]	50.0	33.0[c]
	CMD-MLIP	388	10.0	40.0 [11.7 + 28.3] [d]	50.0	29.2[d]
	CMD-MLIP	3104	10.0	40.0 [– + –]	50.0	–
NVP28	Exp.[g]	–	28.5	43.0 [5.6 + 37.4] [f]	28.5	13.02[f]
	s-BOMD	405	28.5	43.0 [7.9 + 35.0] [b]	28.5	18.37[b]
	CMD-BMP	405	28.5	43.0 [6.5 + 36.4] [c]	28.5	15.12[c]
	CMD-MLIP	405	28.5	43.0 [6.5 + 36.4] [d]	28.5	15.12[d]
	CMD-MLIP	3240	28.5	43.0 [– + –]	28.5	–

[a]From Hoppe et al.[3] [b]Estimated by spin topology distribution at DFT/PBE0 level.[1,2] [c]Defined by composition based on different potential parameters assignment. [d]Estimated by spin topology distribution at DFT/PBE0 level on sampled MLIP configurations. [e]This work. [f]Estimated by XPS.[1] [g]From our previous work.[1]

1.3 BOMD and CMD simulations details

1.3.1 BOMD

BOMD simulations were performed using the Born-Oppenheimer scheme, with atom-centered Gaussian-type basis functions to describe the orbitals, and an auxiliary plane-wave basis set to re-expand the electron density. We employed double-ζ polarized MOLOPT basis sets[9] for Na, V, P, and O, and used a cutoff energy of 800 Ry for the plane waves at the Γ point only. Using the CMD-derived structures (BMP-shrm) as a starting point, the *s*-BOMD models were obtained by a relatively short equilibration by BOMD simulation at 300 K for approximately 5 ps using Goedecker–Teter–Hutter pseudopotentials to describe core-valence interactions[10] together with the semilocal Perdew-Burke-Ernzerhof (PBE)[11,12] exchange–correlation functional within a spin unrestricted DFT formalism. For these *s*-BOMD models, the last 3 ps of the trajectories were used and the results averaged over the three replicas. The final electronic structure was optimized using the PBE0 hybrid functional[13], with 25% Hartree-Fock exchange and a cutoff energy of 800 Ry, to accurately describe the electronic structure, bandgap, and spin topology[14], in line with previous studies.[1,2]

The NVP10 glass *f*-BOMD model was obtained by performing a full thermal cycle at the BOMD level with PBE exchange correlation functional and GTH pseudopotential (as previously performed for *s*-BOMD). We emphasize that *f*-BOMD allows for full relaxation and captures fast dynamical rearrangements that occur during melting and cooling-periods during which many chemical bonds are continuously forming and breaking-enabling an unbiased description of structural features beyond the short range. In contrast, *s*-BOMD involves a relatively short equilibration of glass structures pre-generated by classical MD. As a result, only the short-range environment is relaxed at the first-principles level, while the medium-range order reflects the limitations of the classical potential. Our approach is consistent with the strategy adopted by Tilocca *etal*.[15], where a full FPMD thermal cycle-using Carr-Parrinello (CPMD) scheme-was shown to be essential for accurately describing a bioactive phosphosilicate glass. In the present case, CPMD is not suitable for Na-V-P-O glasses due to the rapid drift in fictitious electronic energy and the early collapse of the ionic-electronic temperature separation, even at moderate temperatures (600 K). This confirms the necessity of using BOMD, which involves recalculating the electronic structure at every step, ensuring accurate energy and force evaluations throughout the simulation.

In the persent case, the *f*-BOMD simulation started with annealing at 0.5 K. The systems were then gradually heated in the NVT ensemble from 300 K up to 3500 K. Melting occurred at 3500 K over 7.9 ps to reach the diffusive regime, as indicated by the MSD profile reported in Fig. S1. Subsequently, the systems were gradually cooled to 300 K with temperature plateau at 2000 K for 9.3 ps, 1200 K for 7.3 ps, 900 K for 7.0 ps, 600 K for 6.0 ps, and finally 300 K for 7.1 ps. This corresponds to an exceptionally high cooling rate of 10^{14} K/s. The necessity for such a high cooling rate arises from the substantial computational cost of BOMD for these NVP systems. Figs. S1 illustrate the thermal cycle and the temporal evolution of the total system energy of the NVP10 system. A slight drift of up to 0.02 % at high temperature (3500 K) is observed, which is attributed to the systematic error inherent in BOMD approach. All BOMD simulations were performed with the CP2K package.[16]

1.3.2 CMD-BMP-shrm

In this work, we employed the force field (FF) schemes previously tested and found to be the most adapted for vanadophosphate glasses.[2] This FF includes PMMCS/BMP-shrm Morse-type two-body potential with P–O–P, P–O–V^{5+}, and V^{5+}–O–V^{5+} three-body potential parameters from ref.[17–20] For this FF we employed the Morse-type interatomic potential named BMP-shrm in ref.[18] which combines

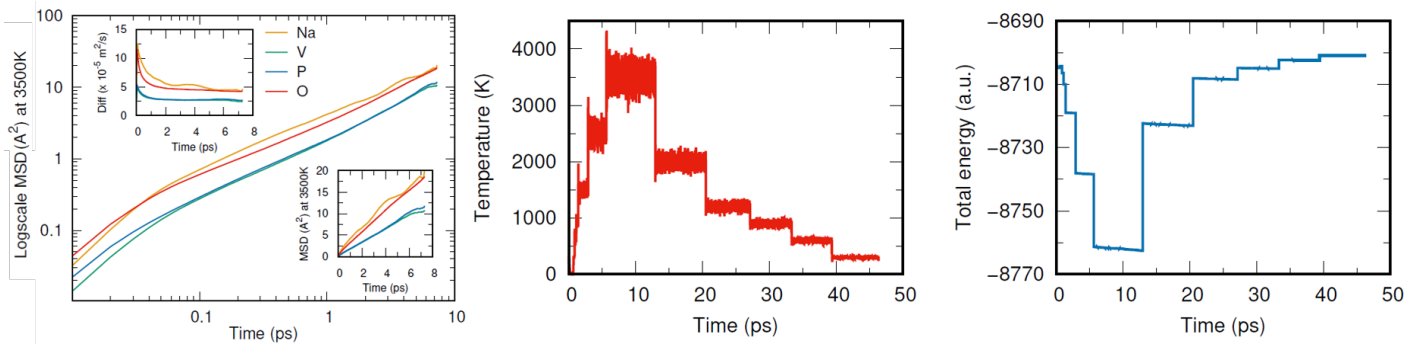

Fig. S1 Left: MSD in logarithmic scale at 3500 K for the NVP10 model. The insets show the diffusion coefficient in cm^2s^{-1} and the MSD in normal scale in Å. Center: Full BOMD thermal cycle performed for the NVP10 glass system. Right: Time evolution of the total energy during the simulation.

the long-range Coulumb interaction, the short-range Morse function and a repulsive term (from the original PMMCS potential, Eq. 1) with the harmonic three-body raster functional (Eq. 2). The two-body potential parameters for V^{5+}-O and V^{4+}-O are taken from ref.[21] This FF employs the three-body potential parameter for the triad P–O–P, P–O–P, P–O–V^{5+}, and V^{5+}–O–V^{5+}, with the latest taken from ref.[20] :

$$U_{ij} = \frac{Z_i Z_j e^2}{r_{ij}} + D_{ij}\left(\left\{1-\exp\left[-a_{ij}(r_{ij}-r_{ij}^0)\right]\right\}^2 - 1\right) + \frac{B_{ij}}{r_{ij}^{12}}, \quad (1)$$

$$U'_{ijk} = \frac{K_{ijk}}{2}\left(\theta_{ijk}-\theta_{ijk}^0\right)^2 \exp\left[-\left(\frac{r_{ij}}{\rho}+\frac{r_{jk}}{\rho}\right)\right] \quad (2)$$

In Table S2 we report the atomic charges used in MD simulations, whereas in Table S3 we report the potential parameters used for each FF, taken from ref.[18,20,21].

Table S2 Atomic charge of different atoms used in classical MD simulations of VP50 glass.

Elements	Na^+	V^{4+}	V^{5+}	P	O
Charges	0.6	2.4	3.0	3.0	-1.2

Table S3 Parameters used for BMP-shrm potential, from ref.[17,18,20,21].

Morse parameters				
Pairs	D_{ij}(eV)	r^0(Å)	a_{ij}(Å^{-2})	B_{ij}(eV Å^{12})
Na^+–O	0.023363	3.006315	1.763867	5.0
V^{4+}–O	0.032832	2.663618	2.109308	1.0
V^{5+}–O	0.021911	3.398507	1.495955	1.0
O–O	0.042395	3.618701	1.379316	100.0
P–O	0.831326	1.790790	2.585833	1.0
Buckingham parameters				
	A_{ij}(eV)		ρ_{ij}(Å^{-2})	
P–P	5.093669		0.905598	
Three-body screened harmonic parameters				
Triplets	K_{ijk}(eV rad^{-2})		θ_0(deg)	ρ (Å)
P–O–P	65.0		109.47	1.0
P–O–V	120.0		109.00	1.0
V–O–V	30.0		109.00	1.0

For CMD-BMP-shrm simulations, the short-range interactions were truncated at a distance of 7.0 Å and the long-range interactions were calculated using the Ewald summation method with a precision of 10^{-5} eV, up to a cutoff distance of 8.5 Å. The velocity Verlet algorithm was employed with a time step of 1 fs to integrate the equation of motion. The NVP glasses models were obtained by melt-quenching thermal procedure[2] with the Nosé-Hoover thermostat[22–24] used to control the temperature. First, the initial structures were relaxed at 300 K in the NVT ensemble. Each system was heated to 4000 K and kept for 150 ps at this temperature followed by the cooling from 4000 K to 300 K with a constant rate of 2.5 K/ps. The relevant properties are averaged over the structures obtained from

the final 150 ps of a 300 ps trajectory at 300 K across different replicas. The CMD-BMP-shrm simulations were performed using the DL-POLY code (version 4.10.0).[25]

1.3.3 CMD-MLIP

We employ a kernel-based MLIP. method using the Gaussian Approximation Potential (GAP) scheme, enabling the learning and reproduction of smooth, high-dimensional potential energy surfaces through the interpolation of DFT data.[26] This MLIP scheme has demonstrated success in various applications, encompassing liquids, crystalline phases, as well as mono and binary glasses.[27,28] However, the application of GAP-type MLIPs to ternary or quaternary amorphous systems remains limited, and to our knowledge, they have not yet been applied to systems containing TMs in different oxidation states. The DFT/BOMD database, which includes a wide range of atomic configurations and corresponding energies, forces, and virials provided the data required for the fitting procedure. By systematically comparing model predictions with database values, we iteratively optimized the potential parameters to achieve the best possible agreement with reference data. In this work, the database is built from two previously generated NVP10 trajectories, which differ in oxygen content and influence the vanadium speciation. These trajectories were produced through a full thermal cycle via f-BOMD simulations using the PBE exchange-correlation functional. Single-point DFT calculations (energy, forces and virials) were performed at the hybrid exchange-correlation functional PBE0 level with a 100 Ry energy cutoff on selected configurations at temperatures of 300, 600, 900, 1500, 2000, 2500, and 3500 K. The database used for MLIP fitting consists of 375 representative configurations, divided into a training set (80% of the total) and a testing set (20% of the total). The optimized GAP hyper-parameters are reported in Table S4.

We validated the accuracy of our GAP model using DFT-BOMD reference data. Figure S2 compares the total energies, atomic forces, and virials predicted by our model with DFT-BOMD results. The GAP model achieves in terms of energy values a relatively low mean absolute error (MAE) of 5.8 meV/atom for the test datasets, fairly in line with the commonly cited high-performance threshold of 5 meV/atom.[29] Forces are predicted with an MAE of 0.4 eV/Å, and virials with an MAE of 16.9 meV/atom. Figure S3 presents cumulative distribution plots of the error distributions. The plots for training and testing datasets align closely and overlap, confirming consistency in predictive performance. Across all three observables, the strong agreement highlights that the MLIP-GAP model accurately represents the first-principles potential energy surface for amorphous NVP.

We employed the fitted GAP potential to produce new models of amorphous NVP10 by following a thermal cycle via canonical NVT simulations, according to the following protocol: heating up from T = 300 K to T = 1500 K , melting at T = 1500 K for 100 ps, cooling from T= 1500 K to T = 300 K with a cooling rate of 2.5 K/ps, and final equilibration at T = 300 K for 300 ps. Subsequent sections present the structural analysis, reported as time-average values over the last 150 ps of the thermal cycles at T= 300 K. The equations of motion were integrated by using a timestep of 1 fs and NH thermostat was used as implemented in the LAMMPS code.[30] Simulations with the developed MLIP were performed in LAMMPS via the QUIP package, which provides support for GAP potentials.[31,32]

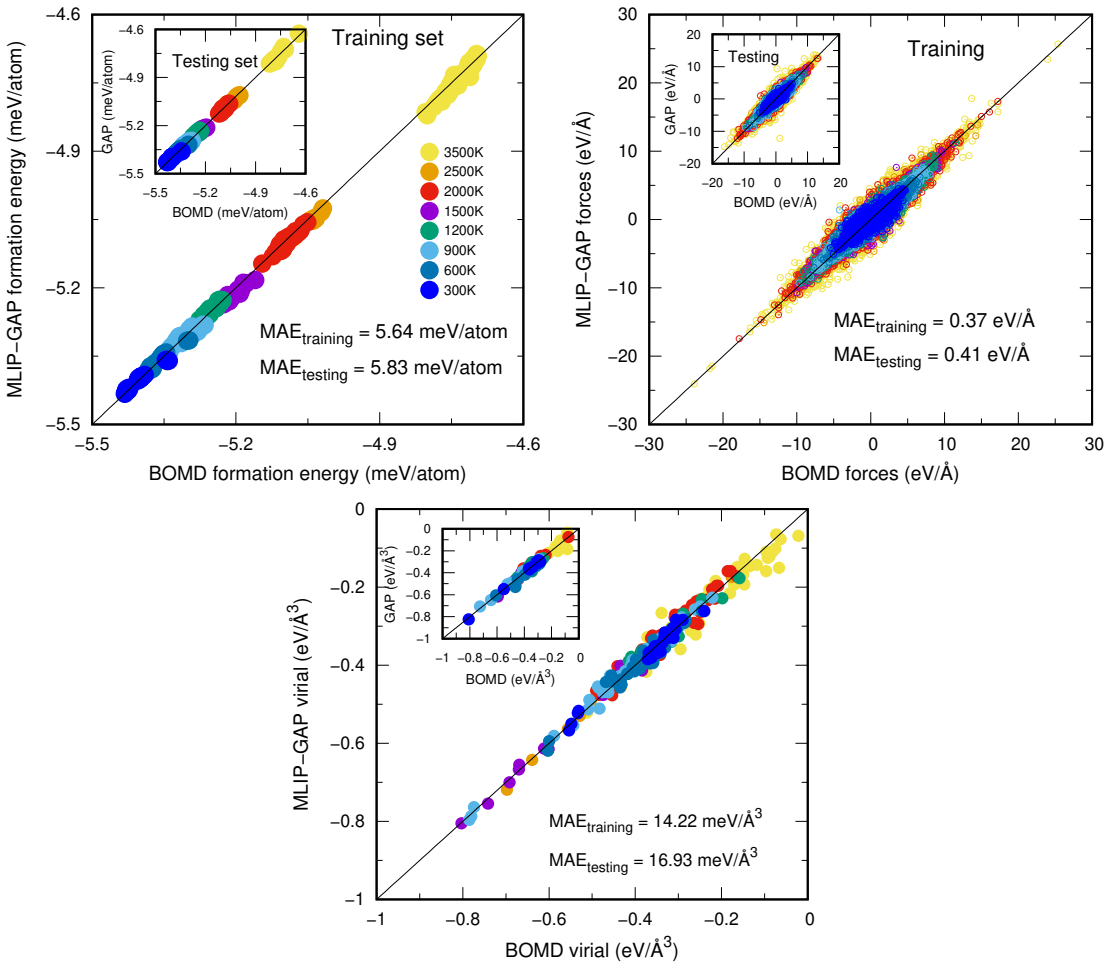

Fig. S2 Scatter plots distributions demonstrating the accuracy and generalization of MLIP predictions. Correlations between DFT-computed and MLIP-predicted energies (Left-top), force components (Right-top), and virials (bottom) for both training and testing sets. Insets magnify the testing data. Mean Absolute Errors (MAE) are provided for each dataset.

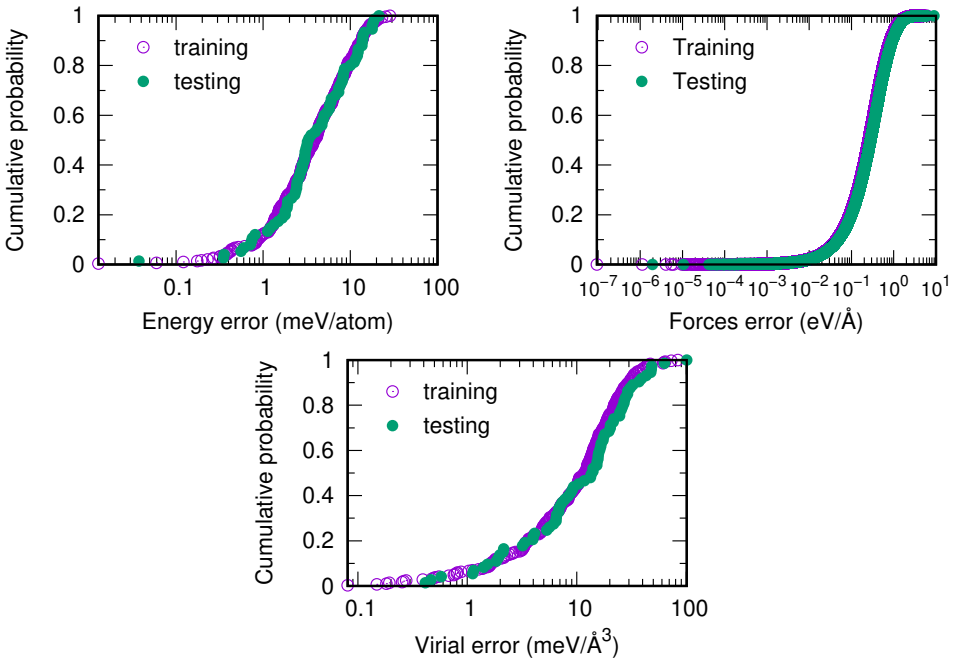

Fig. S3 Cumulative error distributions for energy (Left) and forces (Right) across training and testing sets, confirming the absence of over-fitting during model training.

Table S4 Optimized hyperparameters of MLIP-GAP.

GAP 2b Descriptor	
Cutoff Å	5.0
δ	1.0
Sparse method	uniform
Covariance	Gaussian
Sparse points	50
SOAP Descriptor	
Cutoff Å	5.0
Cutoff width Å	1.0
δ	0.2
Sparse method	CUR POINTS
Sparse points	2772
l_{max}	5.0
n_{max}	8.0
ζ	4.0
Number of descriptors	
2b descriptors	
Na-Na	3582
Na-V	28576
Na-P	39678
Na-O	178488
V-V	44332
V-P	153292
V-O	730238
P-P	80212
P-O	881668
O-O	1916618
SOAP descriptors	
Na	3445
V	13777
P	17221
O	78261
Regularisation	
σ_e (eV)	0.01
σ_f (eV/Å)	0.02
σ_v (eV)	0.02
Database Size and composition, 80% training set.	
Temperature	Number of configurations
300 K	49
600 K	47
900 K	57
1200 K	40
1500 K	20
2000 K	70
2500 K	20
3500 K	57
Total	360
Mean Absolute Error (MAE)	Training *vs* Testing
Energies (meV/atom)	5.64 *vs* 5.83
Forces (eV/Å)	0.37 *vs* 0.41
Virials (meV/atom)	14.22 *vs* 16.93

1.4 Sim. vs Exp. comparative analysis of structural properties

The experimental X-rays reduced total pair distribution function $G(r)$ for NVP10 and NVP28 were obtained as Fourier transform of the total structure factors (see Eq. (3)).

$$G(r) = \frac{2}{\pi}\int_0^{k_{\max}} k\,[S(k)-1]\sin(kr)\,dk \tag{3}$$

These are compared with the calculated $G(r)$ obtained using Eq. (4):

$$G(r) = 4\pi r\rho\,[g_{\mathrm{tot}}(r)-1]\,, \tag{4}$$

where ρ is the number density and $g_{\mathrm{tot}}(r)$ is the unitless total pair correlation function ($g_{\mathrm{tot}}(r) \to 1$ for $r \to \infty$).
For NVP0 system, the experimental total correlation function T(r) (see Eq. (5)) were obtained by Fourier transform of the total structure factor $S(k)$ (X-ray or neutron measurements) [3].

$$\begin{aligned} T(r) &= 4\pi\rho r \;+\; \frac{2}{\pi}\int_0^{k_{max}} k\;[S(k)-1]\sin(kr)\,dk \\ &= 4\pi\rho r + G(r) \end{aligned} \tag{5}$$

Table S5 Comparison of the agreement between CMD, *s*-BOMD, *f*-BOMD, and MLIP simulations and experimental data using goodness-of-fit R_χ parameters for X-rays reduced total pair distribution function $G(r)$ for NVP10 and NVP28 and X-rays and neutron total pair correlation function $T(r)$ for NVP0 at 300 K.

		CMD	*s*-BOMD	*f*-BOMD	MLIP	
		small model[a]	small model[a]	small model[a]	small model[a]	large model[a]
NVP0	$R_\chi^{T^X(r)}$	36.6±0.3	28.7±0.3	-	24.4±0.2	23.8±0.1
	$R_\chi^{T^N(r)}$	26.7±0.1	28.6±0.5	-	25.1±0.1	23.2±0.1
NVP10	$R_\chi^{G^X(r)}$	90.6±1.5	74.1±0.4	58.9±0.5	72.5±1.9	70.7±0.1
NVP28	$R_\chi^{G^X(r)}$	96.2±3.1	65.0±4.8	-	70.9±0.9	65.9± 0.2

[a] Small model: ∼405 atoms; Large models: ∼3104 atoms for NVP10, ∼3240 atoms for NVP28, and ∼5900 atoms for NVP0.

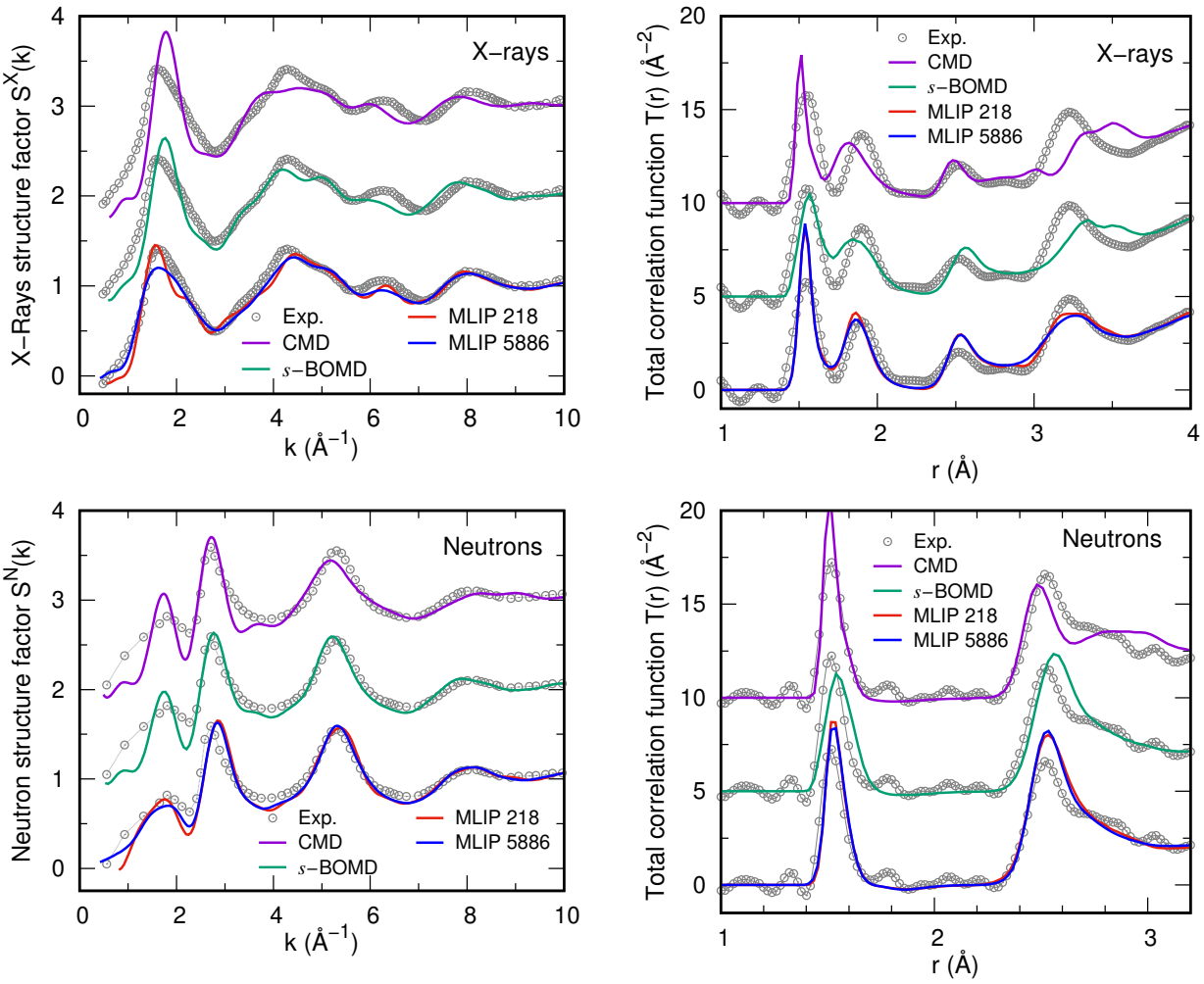

Fig. S4 (Color online) Comparison of experimental and calculated data for NVP0 glass. The top row presents the X-ray total structure factors (left) and pair correlation functions (right), while the bottom row shows the neutron total structure factors (left) and pair correlation functions (right). The calculated results, including CMD, *s*-BOMD and MLIP (for two model sizes, atom counts indicated; curves shifted for clarity) are shown alongside experimental data.

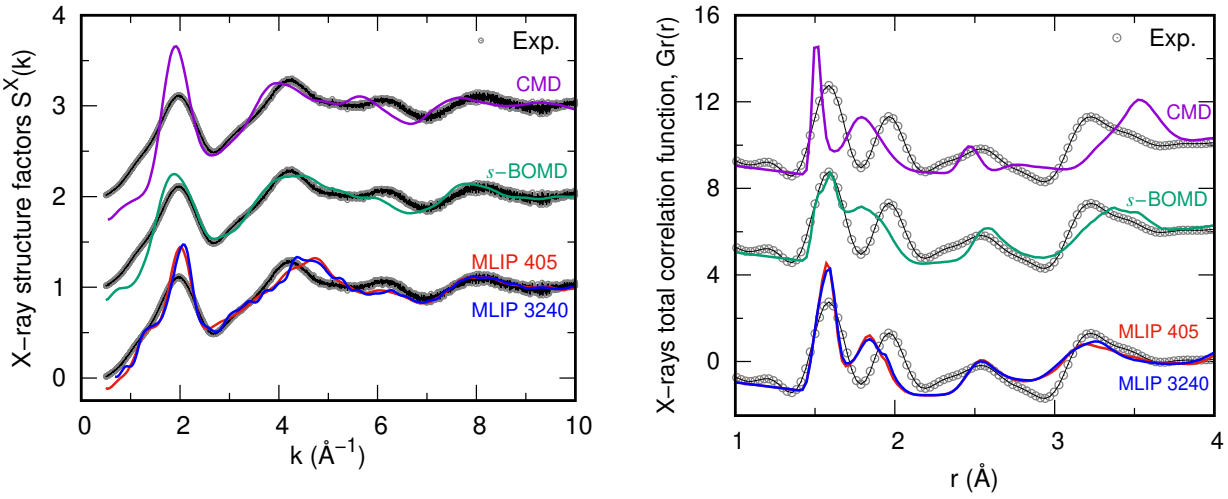

Fig. S5 Total structure factors (Left) and reduced pair correlation function (Right) for NVP28 glasses obtained from X-ray diffraction. Data includes experimental measurements and simulation results (CMD, *s*-BOMD, and MLIP (for two model sizes, atom counts indicated)).

1.5 Computational costs comparative analysis

Table S6 Computational cost for BOMD and CMD simulations for obtaining NVP10 glass.

	f-BOMD	CMD-BMP-shrm	CMD-MLIP	
System size (atoms)	388	388	388	3104
Cubic box length (Å)	17.64	17.64	17.64	35.29
Integration time step (fs)	1	1	1	1
Number of cores (CPU)	320	24	168	336
Time for one iteration (s)	295.45	0.02	0.54	1.30
Cost for one step (h/mpc)	26.26	1.3×10^{-4}	0.03	0.12
Cost for 100 ps (h/mpc)	2.63×10^{6}	13.33	2.51×10^{3}	1.25×10^{4}
Cost to obtain a glass (h/mpc)	1.76×10^{6}	2.67×10^{2}	1.51×10^{4}	7.51×10^{4}
HPC centers	HPE SGI 8600 14PF Jean Zay, IDRIS – GENCI	Intel Cascade Lake with Mellanox Infiniband 100 Gbp, Pole HPC ÉquipeMeso of the University of Strasbourg		

1.6 Glass transition temperature and ionic conductivity determined by computational simulation

The glass transition temperature (T_g) was determined as the intersection of two extrapolated linear fits from the temperature-specific volume (T-V) curves obtained through molecular dynamics simulations in the NPT ensemble. The simulations employed a Nosé-Hoover thermostat and barostat with a heating rate of 4.5 K/ps. The BMP and MLIP interatomic potentials were used to model the NVP28 glass. We present results for both small and large system sizes, consisting of 405 atoms and 3240 atoms, to analyze the effect of system size and potential choice on the estimated T_g.

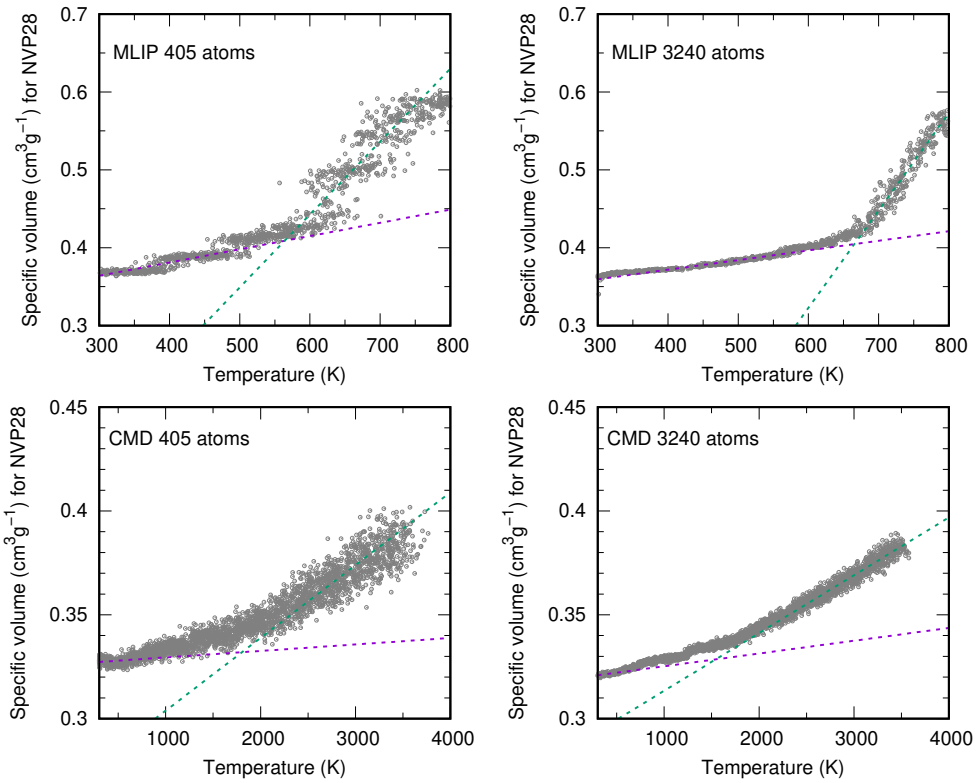

Fig. S6 Glass transition temperature for NVP28 glass simulated by CMD-BMP and CMD-MLIP: small model (405 atoms) $Tg_{0.4k}$ = 540 K (MLIP) *vs* = 1650 K (BMP) and big model (3240 atoms) Tg_{3k} = 640 K (MLIP) *vs* = 1500 K (BMP).

To evaluate the ionic conductivity contribution of the glass through MD simulations, it is necessary to compute the diffusion coefficient, which can be obtained from the slope of the mean square displacement (MSD) as a function of simulation time. The temperatures at which conductivity is experimentally measured are too low to be directly used in MD simulations, as no significant Na-ion jumps (and thus insufficient diffusion) are observed within the accessible simulation timescales of a few nanoseconds. Therefore, the NVT-MD simulation temperatures were set to 1000, 1100, 1200, and 1300 K. Through fitting and extrapolation, the conductivity value at 473 K (the temperature at which multiple experimental data points are available) was estimated, corresponding to the ionic conductivity contribution to the total conductivity. Notably, as discussed in the manuscript, the total experimentally measured conductivity also includes the electronic contribution, which arises from small polaron hopping between V sites with different oxidation states. This electronic contribution is the major component in NVP28 glass. As an example, the MSD up to 3.5 ns of Na ions in the NVP28 glass is shown in Figure 4 of the manuscript, where a dual population of Na ions is evident: one group remains nearly frozen around equilibrium positions (trapped ions), while the other exhibits significant mobility (highly mobile ions), indicative of a diffusive regime. In the diffusive regime, the linear increase of the MSD allows for the determination of the diffusion coefficient. The diffusion coefficient is extracted from the slope of the linear region of the MSD curve, considering only the Na ions that contribute to diffusion. The detailed computational procedure for computing the diffusion coefficients, ionic mobilities, and conductivities follows the approach reported in the computational details of Pham et al[33].

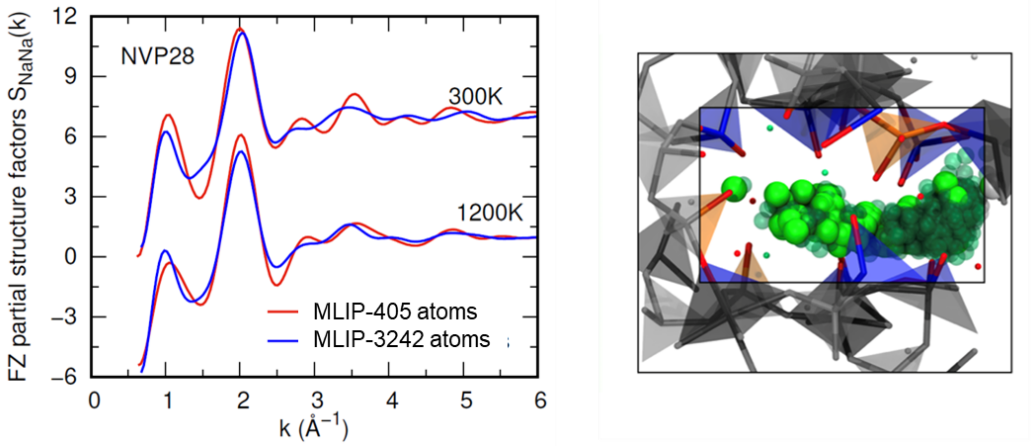

Fig. S7 Left: Faber-Ziman Na-Na partial $S_{\mathrm{NaNa}}(k)$ for small and large NVP28 models at 300 K and 1200K . Right: A percolation channel is shown, highlighting Na-ion interaction with neighboring BOs and NBOs.

1.7 Experimental characterization of NVP28 glass

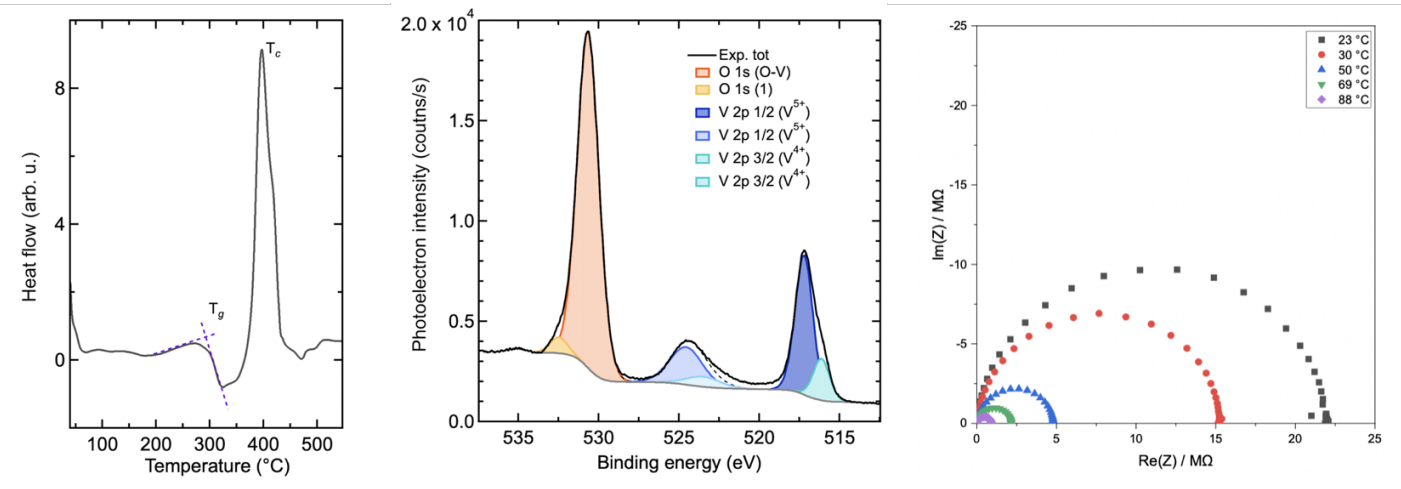

Fig. S8 Left: DSC plot of NVP28 glass showing the glass transition (T_g) and crystallization (T_c) temperatures. Centre: XPS spectrum of NVP28 glass in the O 1s and V 2p regions, revealing the presence of V^{5+} and V^{4+} oxidation states. Right: EIS-derived Nyquist plots at various temperatures of NVP28 glass.

Notes and references

1 S. Wansi Wendji *et al.*, *J. Non-Cryst. Solids*, 2025, **655**, 123420.
2 S. Wansi Wendji *et al.*, *J. Non-Cryst. Solids*, 2024, **634**, 122967.
3 U. Hoppe *et al.*, *J. Non-Cryst. Solids*, 2012, **358**, 328–336.
4 N. Fairley *et al.*, *Appl. Surf. Sci. Adv.*, 2021, **5**, 100112.
5 M. Micoulaut *et al.*, *Phys. Rev. B*, 2023, **108**, 144205.
6 O. Masson, *PYTSREDX: a data reduction program to obtain the atomic pair distribution function (PDF) from X-ray total scattering data*, 2022.
7 *DabaxFiles*, `http://ftp.esrf.fr/pub/scisoft/xop2.3/`, 2024.
8 A. K. Soper and P. Egelstaff, *Nucl. Instrum. Methods*, 1980, **178**, 415–425.
9 J. VandeVondele and J. Hutter, *J. Chem. Phys.*, 2007, **127**, 114105.
10 S. Goedecker, M. Teter and J. Hutter, *Phys. Rev. B*, 1996, **54**, 1703.
11 M. Ernzerhof and G. Scuseria, *J. Chem. Phys.*, 1999, **110**, 5029.
12 M. Seth and T. Ziegler, *J. Chem. Theory Comput.*, 2012, **8**, 901.
13 C. Adamo and V. Barone, *J. Chem. Phys.*, 1999, **110**, 6158–6170.
14 A. Saúl and G. Radtke, *Phys. Rev. B*, 2014, **89**, 104414.
15 A. Tilocca, *Phys. Rev. B*, 2007, **76**, 224202.
16 T. Kühne *et al.*, *J. Chem. Phys.*, 2020, **152**, 1194103.
17 A. Pedone *et al.*, *J. Phys. Chem. B*, 2006, **110**, 11780–11795.
18 M. Bertani *et al.*, *Phys. Rev. Mater.*, 2021, **5**, 045602.
19 A. Pedone *et al.*, *J. Non-Cryst Solids X*, 2022, 100115.
20 G. Malavasi and A. Pedone, *Acta Mater.*, 2022, **229**, 117801.
21 G. Ori *et al.*, *J. Non-Cryst. Solids*, 2011, **357**, 2571–2579.
22 S. Nosé, *J. Chem. Phys*, 1984, **81**, 511–519.
23 W. Hoover, *Phys. Rev. A*, 1985, **31**, 1695.
24 C. Massobrio *et al.*, *Phys. Status Solidi B*, 2023, **261**, 2300209.
25 I. Todorov *et al.*, *STFC, STFC Daresbury Laboratory, Daresbury, Warrington, Cheshire, WA4 4AD, United Kingdom, version*, 2011, **4**, year.
26 A. P. Bartók *et al.*, *Phys. Rev. Lett.*, 2010, **104**, 136403.
27 G. Delaizir *et al.*, *Phys. Chem. Chem. Phys.*, 2020, **22**, 24895–24906.
28 V. L. Deringer *et al.*, *Chem. Rev.*, 2021, **121**, 10073–10141.
29 G. Sivaraman *et al.*, *Npj Comput. Mater.*, 2020, **6**, 104.
30 A. Thompson *et al.*, *Comput. Phys. Commun.*, 2022, **271**, 108171.
31 G. Csányi *et al.*, *IoP Comput. Phys. Newsletter*, 2007, Spring 2007.
32 J. R. Kermode, *J. Phys. Condens. Matter*, 2020.
33 T.-L. Pham *et al.*, *J. Mater. Chem. A*, 2023, **11**, 22922.